IMPROVED NUMERICAL SIMULATION AGAINST OVERFLOW FROM EMBANKMENT UNDER STEADY AND UNSTEADY FLOW CONDITIONS BY CONSIDERING NON-HYDROSTATIC PRESSURE

YOSHIYA IGARASHI
Graduate School of Science and Engineering, Saitama University, Saitama, Japan, igarashi.y01@gmail.com

NORIO TANAKA
International Institute for Resilient Society, Saitama University, Saitama, Japan, tanaka01@mail.saitama-u.ac.jp

ABSTRACT

High accuracy simulation of overtopping flow from an embankment is required. It helps in better understanding the inundation volume and house-breaking situation. When tsunami inundation is simulated on a real scale, wide area, two-dimensional non-linear long-wave equation model (hydrostatic pressure theory) is often used, as CPU time is not large. In this study, an improved method is proposed. This method can simulate tsunami-like flow with non-hydrostatic pressure theory and has almost the same computational load with the non-linear long-wave equation model. Although the method itself can be applied to two-dimensional flow, the method was tested on a one-dimensional depth-averaged non-hydrostatic equation. Comparing the results from unsteady flow flume experiments, the stability of the improved method, the accuracy of overtopping volume from the embankment and the flow depth around the embankment was confirmed. In addition, in order to verify the influence of non-hydrostatic pressure term, a non-linear long-wave equation with the hydrostatic pressure approximation was compared with the improved method, with the non-hydrostatic pressure. It was found that the hydrostatic pressure theory underestimated the overtopping volume from an embankment by about 15% when the width of the top of embankment is narrow. Simulation results of fluid force index, (squared velocity times flow depth) that indicates the probability destruction of houses, are compared with flume experiment results and shown to be highly accurate.

Keywords: Piezometric head, overtopping flow, tsunami inundation, flow rate, embankment modelling

1. INTRODUCTION

After the 2011 Great East Japan tsunami, the Ministry of Land, Infrastructure, Transport and Tourism (MLIT), Japan classified tsunamis into two levels, based on the recurrence period (MLIT, 2011). The recurrence period of the magnitude for the largest tsunamis, level 2 tsunamis, are within one hundred and several decades to a thousand years. The policy of level 2 tsunami countermeasures is to protect human life by using multiple defense systems that mobilizes all countermeasures, both the hard measures, such as elevating the roads behind sea embankment, and the soft measures, such as evacuation plans. After the 2011 tsunami, multiple defense system against a level 2 tsunami is planned on some places in Japan (Strusinska-Correia 2017). Also, experimental studies about multiple defense system consisted of sea embankment and coastal forest (Igarashi and Tanaka, 2016), lined piles (Igarashi et al., 2018), and second embankment (Tanaka and Igarashi, 2016) have conducted, and effectiveness of multiple defense system is becoming more apparent. However, various cases need to be considered when planning the countermeasures on the real world in the case of a level 2 tsunami. Therefore, it is necessary to analyze the flow around the sea embankment accurately. This is because the calculation accuracy of the overtopping flow rate from sea embankment and the flow inland from the embankment greatly affects the estimation of the flood area and the probability of house destruction.

The flow over the embankment has a non-hydrostatic pressure, especially, at the top and at the toe of embankment because the vertical velocity is not negligible. The non-linear long-wave equations, which are often used in wide-area inundation analysis, use the hydrostatic pressure approximation. Therefore, the accuracy of calculating the flow level around embankment and overflow volume from embankment is low. For this reason, researches have been using the Boussinesq equation that introduces a non-hydrostatic pressure term caused by a vertical acceleration, in their simulation. However, the introduction of the non-hydrostatic pressure term tends to generate non-physical oscillation on the water surface. Therefore, various calculation schemes to suppress the oscillation was used. Moreover, an implicit method was used. Therefore, these numerical simulation methods have problems in terms of calculation load and stability of analysis for unsteady flow. Therefore, the

purpose of this study was to develop a numerical simulation method that considers the non-hydrostatic pressure term except for the time derivative term. In order to verify the accuracy of the developed analysis method, comparison with previous studies (Honma ,1940; Fritz and Hager ,1998; Ikezawa et al, 2015) and flume experiments are elucidated.

2. MATERIAL AND METHOD

2.1 Equations

Navier-Stokes equation in x and z direction are shown in Equation (1) and (2), respectively.

$$\frac{\partial u}{\partial t}+u\frac{\partial u}{\partial x}+v\frac{\partial u}{\partial y}+w\frac{\partial u}{\partial z}+\frac{1}{\rho}\frac{\partial p}{\partial x}-\frac{1}{\rho}\left(\frac{\partial \tau_{xx}}{\partial x}+\frac{\partial \tau_{yx}}{\partial y}+\frac{\partial \tau_{zx}}{\partial z}\right)-F_x=0 \tag{1}$$

$$\frac{\partial w}{\partial t}+u\frac{\partial w}{\partial x}+v\frac{\partial w}{\partial y}+w\frac{\partial w}{\partial z}+\frac{1}{\rho}\frac{\partial p}{\partial z}-\frac{1}{\rho}\left(\frac{\partial \tau_{xz}}{\partial x}+\frac{\partial \tau_{yz}}{\partial y}+\frac{\partial \tau_{zz}}{\partial z}\right)+\mathrm{g}-F_z=0 \tag{2}$$

where, u, v, and w are flow velocities in x, y, and z direction, respectively. t is time. ρ is the density of the fluid, g is the gravitational acceleration, and p is the pressure. τ is the shear stress, and the subscript indicates the position and direction of action. F is the external force, and the subscript indicates the direction.

In order to calculate the pressure at an arbitrary height z, equation (2) is changed to the dimensionless equation, and the fifth term on the left side is integrated from the water surface to the arbitrary height z^* equation (3) is calculated.

$$[p]_{z^*}=(\varepsilon\zeta^*-z^*)-\sigma\int_{\varepsilon\zeta^*}^{z^*}\frac{Dw^*}{Dt^*}dz^* \tag{3}$$

where ε is the wave height ratio (ζ_0/h_0) and σ is the relative water depth (${h_0}^2/{l_0}^2$). l_0 and h_0 are the representative lengths (m) in the horizontal and vertical directions, respectively, and ζ_0 is the representative length (m) corresponding to the wave height. Equation (3) was calculated by using the assumption $\varepsilon^2 \ll 1$. Variables marked with * represents non-dimensional value. ζ^* is a non-dimensional flow level from the reference height.

Equation (1) is changed to a non-dimensional equation, and the pressure term of the fifth term on the left-hand side is integrated from bed to water surface, and equation (4) is calculated.

$$\int_{-h^*}^{\varepsilon\zeta^*}\frac{\partial p^*}{\partial x^*}dz^*=\varepsilon(\varepsilon\zeta^*+h^*)\frac{\partial \zeta^*}{\partial x^*}-\sigma\frac{\partial}{\partial x^*}\int_{-h^*}^{\varepsilon\zeta^*}\int_{\varepsilon\zeta^*}^{z^*}\frac{Dw^*}{Dt^*}dz^*\,dz^*-\sigma\frac{\partial h^*}{\partial x^*}\int_{-h^*}^{\varepsilon\zeta^*}\frac{Dw^*}{Dt^*}dz^* \tag{4}$$

Next, to calculate the vertical velocity $[w^*]_{z^*}$ at an arbitrary height z, the continuity equation (5) is changed to the non-dimensional equation and integrated vertically from the bottom ($-h^*$) to an arbitrary height (z^*). Moreover, partial differentiation of $[w^*]_{z^*}$ with t^*, x^*, and z^*, are calculated, and Dw^*/Dt^* is calculated, as shown in equation (6).

$$\frac{\partial u}{\partial x}+\frac{\partial v}{\partial y}+\frac{\partial w}{\partial z}=0 \tag{5}$$

$$\frac{Dw^*}{Dt^*}=-\varepsilon(z^*+h^*)\left\{\frac{\partial^2\bar{u}^*}{\partial t^*\partial x^*}+\varepsilon\bar{u}^*\frac{\partial^2\bar{u}^*}{\partial {x^*}^2}-\varepsilon\left(\frac{\partial\bar{u}^*}{\partial x^*}\right)^2\right\}-\varepsilon\left\{\frac{\partial}{\partial t^*}\left(\bar{u}^*\frac{\partial h}{\partial x^*}\right)+\varepsilon\bar{u}^*\frac{\partial}{\partial x^*}\left(\bar{u}^*\frac{\partial h^*}{\partial x^*}\right)\right\}+O(\sigma) \tag{6}$$

where $\bar{u}^*$ is the non-dimensional cross-sectional average flow velocity in x-axis direction. In addition, equation (6) was calculated by assuming that $\partial h/\partial t=0$. From equations (4) and (6), the water depth integral of the pressure term can be calculated without using the vertical velocity w, converted back to a dimensional equation, equation (7) is calculated.

$$\int_{-h}^{\zeta}\frac{\partial p}{\partial x}dz=\mathrm{g}D\frac{\partial \zeta}{\partial x}-\frac{\partial}{\partial x}\left[\frac{D^3}{3}F_1+\frac{D^2}{2}F_2\right]+\frac{\partial h}{\partial x}\left[\frac{D^2}{2}F_1+DF_2\right] \tag{7}$$

Here, D is the total flow depth, and F_1 and F_2 are expressed by equations (8) and (9), respectively. These equations were used in the paper (Ikezawa et al, 2015).

$$F_1=\frac{\partial^2 u}{\partial t\partial x}+u\frac{\partial^2 u}{\partial x^2}-\left(\frac{\partial u}{\partial x}\right)^2 \tag{8}$$

$$F_2=\frac{\partial}{\partial t}\left(u\frac{\partial h}{\partial x}\right)+u\frac{\partial}{\partial x}\left(u\frac{\partial h}{\partial x}\right) \tag{9}$$

Here, the time derivative term, which affects only the unsteady flow, is the main factor that causes non-physical oscillations is ignored in this paper. Therefore, equations (8) and (9) changed to equations (10) and (11), respectively.

$$F_1' = u\frac{\partial^2 u}{\partial x^2} - \left(\frac{\partial u}{\partial x}\right)^2 \tag{10}$$

$$F_2' = u\frac{\partial}{\partial x}\left(u\frac{\partial h}{\partial x}\right) \tag{11}$$

Equations (12) and (13) show the water-depth-averaged continuity equation and momentum equation, respectively.

$$\frac{\partial \zeta}{\partial t} + \frac{\partial q}{\partial x} = 0 \tag{12}$$

$$\frac{\partial q}{\partial t} + \frac{\partial}{\partial x}\left(\frac{q^2}{D}\right) + \frac{gn^2}{D^{7/3}}q|q| - 2\frac{\partial}{\partial x}\left(\nu_e\frac{\partial q}{\partial x}\right) + gD\frac{\partial \zeta}{\partial x} - \frac{\partial}{\partial x}\left[\frac{D^3}{3}F_1 + \frac{D^2}{2}F_2\right] + \frac{\partial h}{\partial x}\left[\frac{D^2}{2}F_1 + DF_2\right] = 0 \tag{13}$$

Here, q is the flow rate in the x-axis direction (m^2s^{-1}), and n is the Manning's roughness coefficient ($m^{-1/3}$·s). ν_e is the eddy viscosity coefficient (m^2s^{-1}), which is calculated spatiotemporally based on the turbulent energy transport equation and turbulent energy dissipation rate due to bed friction and flow velocity difference in the x-axis direction (Nadaoka and Yagi, 1998).

2.2 Calculation scheme

The staggered grid was used for discretization in the spatial direction, and the leapfrog method was used for discretization in the time direction. For the difference in the time direction between Equations (12) and (13), the first-order precision forward difference was used, and the first-order accuracy upwind difference was used for the advection term in Equation (2). The difference in the x-direction of the other terms was the first-order precision central difference. For the bed friction term in Equation (2), the Crank-Nicholson method was used. The transport equation of the turbulent energy is also a first-order accuracy central difference. Ikezawa et al. (2015) used an implicit method for calculating non-hydrostatic pressure terms. However, this study, the explicit method was used for calculating non-hydrostatic pressure terms. Therefore, this model can simulate including the effect of non-hydrostatic pressure term and have an almost same computational load as the non-linear long-wave equation model.

For calculation of the wave tip, the slip condition was used as in Kawasaki et al. (2004). However, this analysis model solves not the flow velocity but the flow rate. Therefore, to calculate $q_{i+1/2}^{n+1}$ at wave tip, Equation (14) was used when $q_{i+1/2}^{n}$ is greater than 0 (positive value represents the right direction in Figure 1), $d_{i+1/2}^{n+1/2}$ is less than D_{min}, and $d_{i-1/2}^{n+1/2}$ is greater than D_{min}. Here, the superscript indicates the calculation time step, and the subscript indicates the grid position in the x-axis direction. D_{min} is the lower limit of the water depth for calculating the momentum, Equation (13), and was set to 1 mm in this numerical simulation.

$$q_{i+1/2}^{n+1} = \frac{q_{i-1/2}^{n}}{d_{i-1/2}^{n+1/2}} \times d_{i+1/2}^{n+1/2} \tag{14}$$

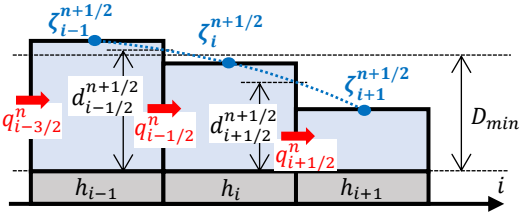

Figure 1. Calculation of the flow rate at the tip of the wave under the SLIP condition and interpolation calculation of the water depth at the flow rate defined position using the QUICK scheme

In this simulation, flow depth, $d_{i+1/2}^{n+1/2}$, at the definition position of flow rate does not calculate the average between $d_i^{n+1/2}$ and $d_{i+1}^{n+1/2}$, instead, a QUICK scheme with second-order accuracy was used, as shown in Equation (15). For example, when $q_{i+1/2}^{n}$ is greater than 0, the quadratic function through $\zeta_{i-1}^{n+1/2}$, $\zeta_i^{n+1/2}$, and $\zeta_{i+1}^{n+1/2}$ was calculated and found by Equation (13).

$$d_{i+1/2}^{n+1/2} = \frac{1}{8}\left(3\zeta_{i+1}^{n+1/2} + 6\zeta_i^{n+1/2} - \zeta_{i-1}^{n+1/2}\right) + h_{i+1/2} \tag{15}$$

However, when the value of $d_{i+1/2}^{n+1/2}$ calculated by Equation (15) is less than $d_i^{n+1/2}$, or greater than $d_{i+1}^{n+1/2}$, $d_{i+1/2}^{n+1/2}$ then it is calculated by the average between $d_i^{n+1/2}$ and $d_{i+1}^{n+1/2}$. This means that $\zeta_{i+1/2}$ calculated by the QUICK scheme becomes larger than both ζ_i and ζ_{i+1} when the water level in x-direction various as shown in Fig.2. Non-physical oscillation occurs from the location i+1/2 if the $\zeta_{i+1/2}$ is used in the momentum equation. Therefore, not QUICK scheme but an arithmetical mean of $d_i^{n+1/2}$ and $d_{i+1}^{n+1/2}$ was used for calculating $d_{i+1/2}^{n+1/2}$ when $\zeta_{i+1/2}$

calculated by QUICK scheme is larger than both ζ_i and ζ_{i+1}. This switch of QUICK scheme and an arithmetical mean to calculate $d_{i+1/2}^{n+1/2}$ ($\zeta_{i+1/2}^{n+1/2}$) made non-physical oscillation small behind the embankment.

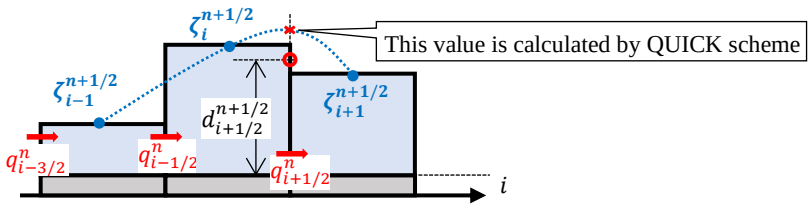

Figure 2. Switch of QUICK scheme and an arithmetical mean to calculate $d_{i+1/2}^{n+1/2}$

2.3 Previous studies for accuracy verification and boundary conditions for numerical simulations

2.3.1 Flow level around embankment

In order to verify the accuracy of overtopping volume from embankment under steady flow, a comparison with the flume experiment of Ikezawa et al. (2015) was conducted. For comparison with the results of this analysis, the data was read from the paper of Ikezawa et al. (2015). The data was converted so that the reading error was ± 0.5 mm in the z-direction at 5 mm intervals in the x-direction.

The width of the top of embankment is 6 cm, an embankment height is 12 cm, and both slopes of the embankment is 1/2. For comparison with the results of numerical simulation by Ikezawa et al. (2015), the same boundary conditions were used. Grid size (DX) is 0.01 m, and *n* is 0.01. In addition, a steady flow was generated by gradually increasing the water level on the upstream side of the embankment and keeping it constant when the overflow water depth reached the target value. The ground level behind the embankment was set horizontally, and simulation was conducted until the water level behind the embankment stabilized. The overflow depth was set as 6 cm.

2.3.2 Overtopping volume from embankment

Honma (1940) showed the experimental equation for overflow per unit width q (m^2s^{-1}) from the weir. Equations (16) and (17) were shown when the cross-section of the weir was rectangular and trapezoidal, respectively. These equations are for complete overflow.

$$q = 0.35(2gh_0^3)^{1/2} \tag{16}$$

$$q = \left(0.31 + 0.23\frac{h_0}{h_a}\right)(2gh_0^3)^{1/2} \tag{17}$$

Fritz and Hager (1998) showed the experimental Equation (18) for the overflow per unit width q (m^2s^{-1}) from the weir that includes the effect of the crest width (L_w) for a 1/2 slope weir.

$$q = C_d(2gH_0^3)^{1/2} \tag{18}$$

$$C_d = 0.43 + 0.06\sin[\pi(R - 0.55)] \tag{19}$$

$$R = \frac{H_0}{H_0 + L_w} \tag{20}$$

Here, C_d is the discharge coefficient and is shown as Equation (19). R is the relative crest length as shown in Equation (20); H_0 the total head and L_w is the crest length.

2.4 Experimental conditions for accuracy verification and numerical simulation conditions for those experiments.

2.4.1 Steady flow experiment

In order to verify the numerical simulation accuracy of the flow level and the fluid force index behind the embankment under steady flow conditions, flume experiments were conducted in a channel, as shown in Figure 3. The width of the top of embankment is 0.12 m, and the embankment height is 0.29 m, and both slopes of the embankment are 1/2. The flow level was measured at three positions (G1, G2, and G3) downstream of the embankment. The measurement positions are 1.6 m (G1), 2.75 m (G2) and 4.75 m (G3) from the toe of the embankment on the land side. In addition, the overtopping volume from embankment was also measured. The non-dimensional overflow water depth was calculated by dividing the critical water depth calculated from the overtopping volume per second by the embankment height. That range is 0.05-0.35.

2.4.2 Numerical analysis condition for steady flow experiments

Grid size (DX) was set to 0.02 m and *n* was set to 0.01 as boundary conditions for this simulation. The method

of generating a steady flow is the same as the method described above. The water level upstream of the embankment was set in 22 cases in the range of 0.3 m to 0.44 m. The non-dimensional overflow water depth was between 0.02 and 0.38.

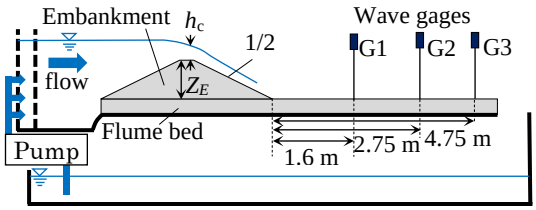

Figure 3. Setup of channel, model and measuring equipment for steady flow experiment

2.4.3 Unsteady flow experiments

Ikezawa et al (2015) mentioned that the non-hydrostatic pressure model has an issue about calculating unsteady flow. This is because water level entirely changes in time, non-physical oscillation quickly occurs. Therefore, the applicability of this non-hydrostatic pressure theory against the unsteady flow was confirmed.

In order to verify the accuracy of the numerical simulation under unsteady condition, a fixed flume bed model and an embankment model were placed in a channel. A tsunami-like flow can be generated by a quickly lifting gate as shown in Figure 4, and the time series of flow level was measured. The water level was measured at G1, G2, and G3 positions in Figure 4 by using a wave gage (HAT-106 (main unit), HAT-30 (detection unit), Tokyo Metrology Co., Ltd.). In this experiment, the width of the top of the embankment was 0.05 m, embankment height was 0.062 m. The initial water depth (H_t) was set as 0.15 m, 0.20 m, and 0.25 m.

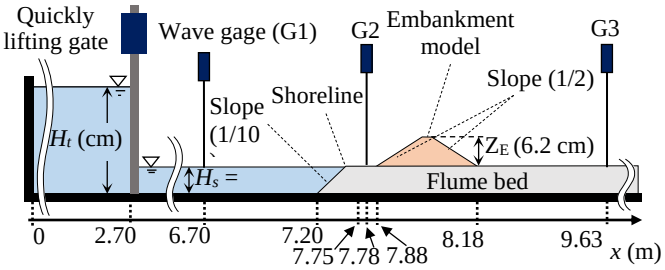

Figure 4. Setup of the channel, model and measuring equipment for unsteady flow experiment

2.4.4 Numerical analysis condition for unsteady flow experiments

In this numerical simulation for unsteady flow, grid size (DX) was set as 0.025 m. The calculation time interval (DT) was set to satisfy the Courant-Friedrichs-Lewy Condition. *n* was set to 0.015 on the tank side (x <7.2 m) from the fixed flume bed, and was set to 0.01 for the fixed floor model because the surface was made of wood and smooth. To generate of the tsunami-like flow by the quickly lifting gate in this simulation, the initial water level in a tank (0 m < x < 2.7 m) according to H_t and initial water level from the gate to flume bed (H_S) were set.

3. RESULTS AND DISCUSSION

3.1 Steady flow

3.1.1 Flow level around embankment

Figure 5 shows the results of the flow level around the embankment.

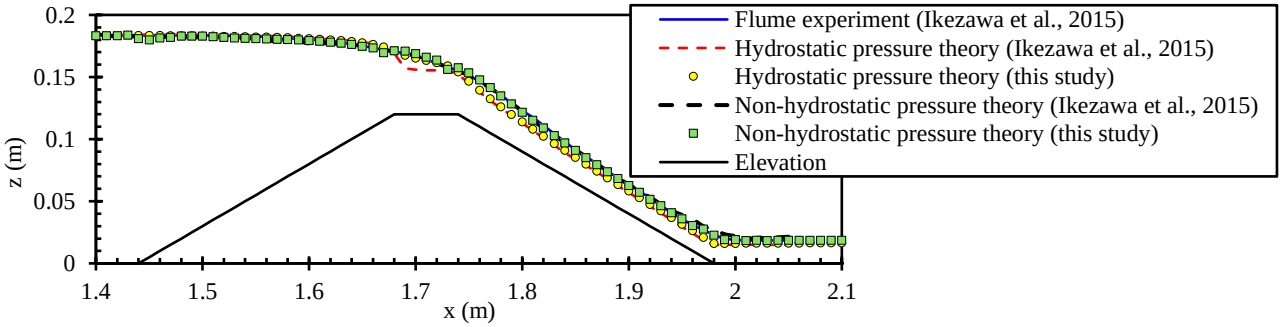

Figure 5. Flow level around embankment

From this figure, the flow level on the landside slope of the embankment calculated by the hydrostatic pressure approximation method is low. However, the flow level calculated by the non-hydrostatic pressure method is almost the same as the experimental result. This result has the same tendency in the simulation results of Ikezawa et al. (2015). This is because the non-hydrostatic pressure (positive pressure) on the landside slope and the

landside toe of embankment reduced the flow velocity. Under this calculation, there was no significant difference between the simulated results in this study and the simulated results of Ikezawa et al. (2015). Ikezawa et al. (2015) considered the time derivative term of non-hydrostatic pressure term and used implicit method to calculate the non-hydrostatic pressure term. On the other hand, this study ignored the time derivative term and used an explicit method to calculate the non-hydrostatic pressure term. However, both results are quite similar. Therefore, the time derivative term can be ignored, and the explicit method can be used.

3.1.2Overtopping volume from embankment

Figure 6 shows the relationship between the discharge coefficient (C_D) and the relative crest length (R), which is the experimental formula between Honma (1940) and Fritz and Hager (1998), the analytical results of Ikezawa et al. (2015), and the analytical results of this study. Since the empirical formula of Honma (1940) does not include the influence of the top width of the weir (L_W), the discharge coefficient is constant. Fritz and Hager's empirical formula includes the effect of the top width of the weir, and the larger the relative top width, the larger the discharge coefficient. According to the analysis results of the hydrostatic pressure approximation, the flow coefficient was almost constant regardless of the value of the relative top width. On the other hand, the non-hydrostatic model can accurately analyze the change of the discharge coefficient due to the change of the relative crown width. This is because the non-hydrostatic pressure generated near the top can be accurately calculated. It indicates that the hydrostatic pressure theory underestimated the overtopping volume from an embankment by about 15% when the top width of the crest of embankment is small.

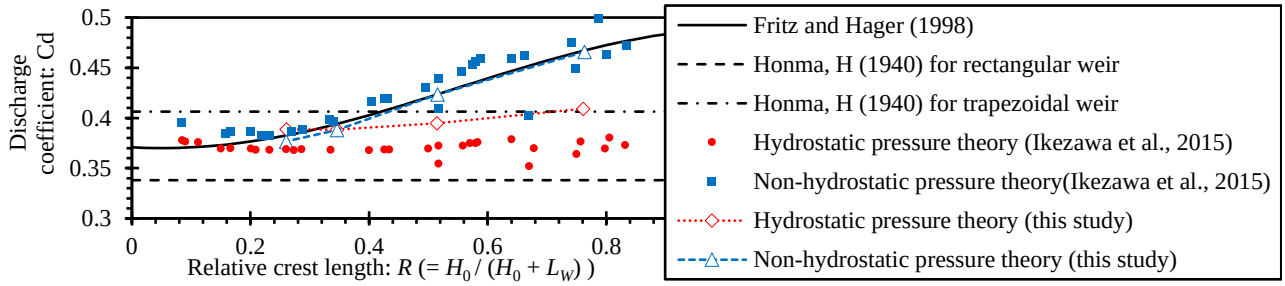

Figure 6. Relationship between discharge coefficient and relative crest length

3.1.3 Fluid force index behind embankment

Drag force on objects, such as houses, coastal forest is calculated by equation (21). This equation can be used to understand the breaking situation. Here, C_D is drag coefficient, u is flow velocities in the x-direction, h is flow depth, ρ is the density of the fluid, and d is the width of objected things. C_D are 1 or 2, and d diameter of tree trunk or width of a house when objected things are tree trunk or house. Therefore, they are the constant values except for flow velocity (u) and flow depth (h), and u^2h is called fluid force index, as shown in equation (22). The fluid force index is often used in understanding house breakage probability (Hayashi et al., 2013).

$$(Drag\ force) = \frac{1}{2} C_D \rho u^2 h d = (constant\ value) \times u^2 h \tag{21}$$

$$(Fluid force\ index) = u^2 h \tag{22}$$

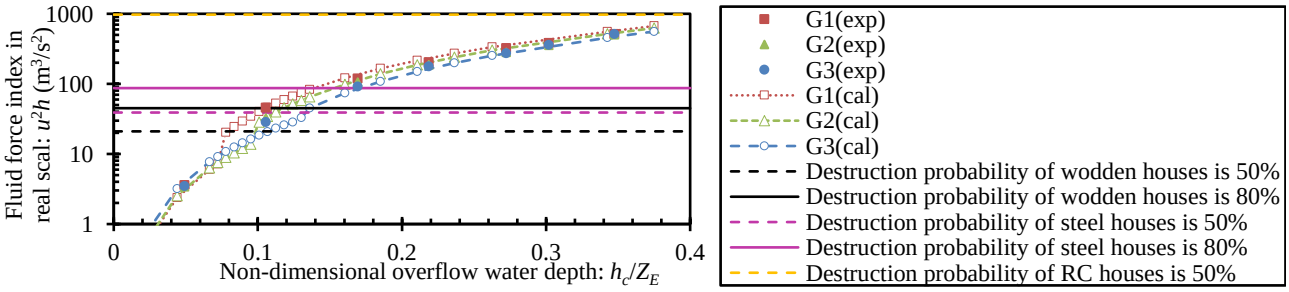

Figure 7. Fluid force index in real scale and destruction probability of houses

Figure 7 shows the experimental and analytical results of the fluid force index converted to the actual scale. The values of 50% or 80% for wooden, steel and RC houses (Hayashi et al., 2013) are also shown for comparison. From this figure, the experimental results and the analytical results of the fluid force index are almost the same. Also, the fluid force index (u^2h) at G1 changes significantly when the non-dimensional overflow water depth increases from about 0.07 to 0.08. This is because of the flow condition at G1 changes. Flow is in supercritical condition at the G1 in this simulation when the h_c/Z_E is less than 0.07, and flow is in a subcritical condition when the h_c/Z_E is more than 0.08. Comparing the simulation results and experimental results at G3, flow condition changed from supercritical flow to subcritical flow when the h_c/Z_E was changed from about 0.05 to 0.1 in the experiment, but the change of flow condition occurs when h_c/Z_E was 0.13 to 0.14 in this numerical

simulation. This means that the location where the hydraulic jump occurs in numerical simulation is farther downstream from the embankment than observed in the experimental result.

3.2 Unsteady flow

3.2.1 Time series of flow level around embankment

Figures 8, 9 and 10 show the experimental results (plot) and numerical simulation results (solid line or broken line) of the time series of flow level at G1, G2, and G3, respectively. The left figure (a) and the right figure (b), in Figures 8-10, show that the tank water depth H_t are 25 cm and 15 cm, respectively. The experiment was conducted three times for each case. Therefore, the three results are shown in different plots. This shows that the reproducibility of this experiment is high. The solid line shows the results calculated by hydrostatic pressure theory, and the broken line shows the results calculated by the non-hydrostatic pressure theory.

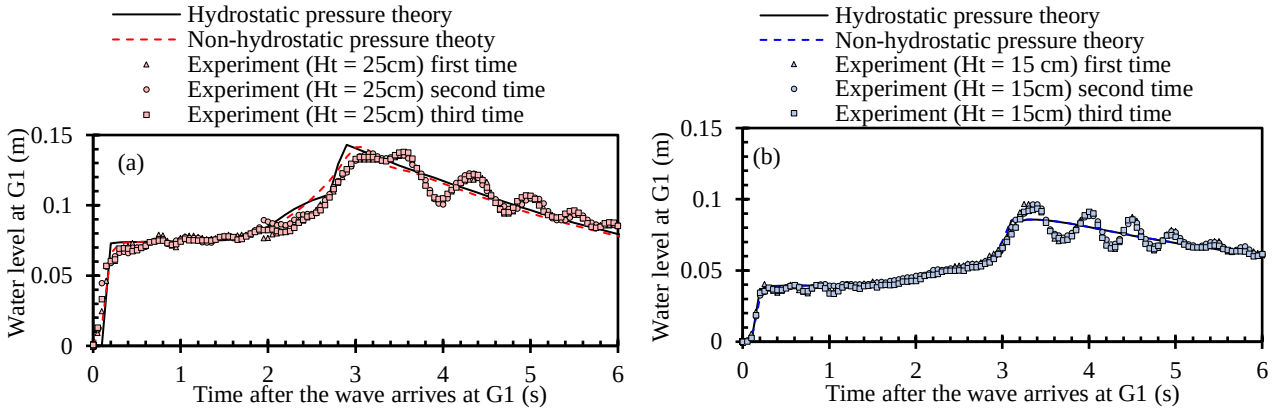

Figure 8. Time series of flow level at G1 ((a): H_t = 25cm, (b): H_t = 15cm)

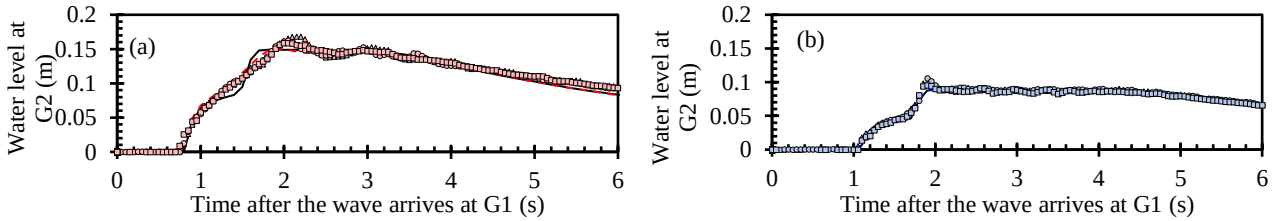

Figure 9. Time series of flow level at G2 ((a): H_t = 25cm, (b): H_t = 15cm)

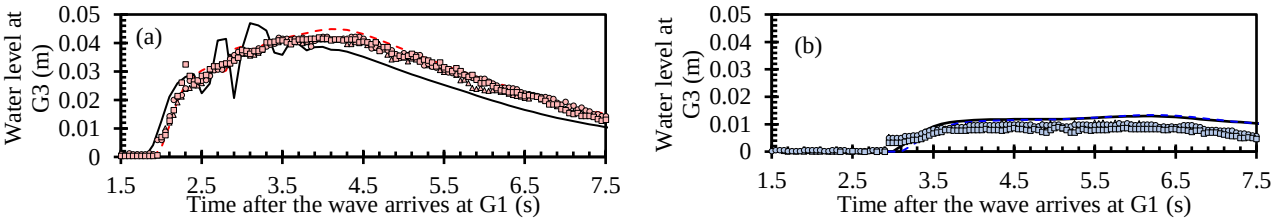

Figure 10. Time series of flow level at G3 ((a): H_t = 25cm, (b): H_t = 15cm)

From Figure 8, the flow level rises rapidly in about 0.2-0.4 seconds due to the arrival of the tsunami-like wave. However, in the hydrostatic pressure theory, especially when the wave height is large, the change of flow level is not smooth, and that rises rapidly in about 0.1 seconds. However, non-hydrostatic pressure theory was able to calculate the rise in flow level accurately. This is because the non-hydrostatic pressure term in this paper includes the effect of the flow velocity difference in the x-axis direction. However, the term of the time derivative is ignored as shown in equations (10) and (11). In addition, the flow level rises again 2-3 seconds after the wave reaches the G1 point due to the reflection by the slope of flume bed. In the experiment, the water surface oscillates in the longitudinal and transverse directions of the channel when the reflection from the slope occurs. In the hydrostatic pressure theory, the change of the flow level due to the reflection from the slope is not smooth, and the water surface oscillation does not occur. On the other hand, in the non-hydrostatic pressure theory, the flow level changes smoothly by reflection from the slope (time is during 2-3 second in Fig.8a), and the oscillation of water surface occurs when H_t is 25 cm (time is during 3-4 second in Fig.8a) although the amplitude of water surface oscillation is small. These differences between non-hydrostatic pressure theory and hydrostatic pressure theory are caused because the non-hydrostatic pressure term includes the effects of the varying flow velocity and ground level in the x-axis direction, as shown in Figure 11. This means the effect of the non-hydrostatic pressure term is important, especially around embankment because of ground level and flow velocity in x-axis direction varies. On the other hand, there are two main reasons why there is a difference between experimental results and hydrostatic pressure theory. One thing is the limitation of this hydrostatic pressure theory due to ignoring the time derivative term of non-hydrostatic pressure term. This means an effect

of the time derivative term is large for flow level oscillation. The other thing is that three-dimensional flow occurs in this flume experiment. Flow level in front of the embankment is various in cross direction, especially when the reflection wave from embankment occurs. Therefore, this simulation results can be more improved when the simulation includes the effect of friction of flume channel sidewall.

In the time series of the flow level at G2 (near the shoreline), the flow level calculated by the non-hydrostatic model smoothly changes over time. That trend is similar to experimental results (Figure 9). In the time series of the flow level behind the embankment, non-physical water surface oscillation is generated in the hydrostatic pressure theory (Figure 10(a)). However, the non-hydrostatic pressure model that considers the terms other than the time derivative term includes changes in the topographic gradient and the effects of longitudinal velocity difference. Therefore, the flow level changes smoothly over time; hence, the calculation's accuracy and stability were improved.

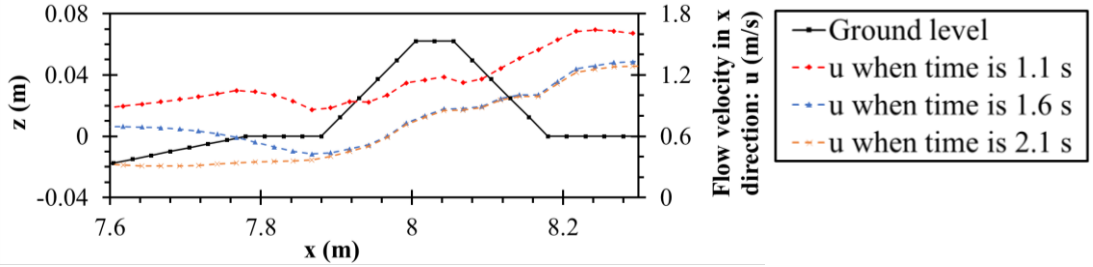

Figure 11. Topographic gradient and the longitudinal velocity differences in H_t = 25cm

4. CONCLUSIONS

The analysis of flow over an embankment was improved by considering the non-hydrostatic pressure, even after ignoring the time derivative. The accuracy of the flow level around the embankment, the overflow, the flow depth behind the embankment, and the stability of unsteady flow in this numerical model were verified through experiments. In steady flow condition, calculated water level around embankment by simplified non-hydrostatic theory and observed water level by flume experiment was quite similar, even after this theory ignored time derivative term and used an explicit method. In addition, the flow level changes smoothly over time because the non-hydrostatic pressure theory considers the changes in the topographic gradient and the effects of longitudinal velocity differences.

ACKNOWLEDGMENTS

This study was supported in part by JSPS KAKENHI Grant Number JP18J11942.

REFERENCES

Igarashi, Y., Tanaka, N. Effectiveness of a compound defense system of sea embankment and coastal forest against a tsunami. Ocean Eng. 151, 246-256, 2018.

Igarashi, Y., Tanaka, N., Zaha, T. Changes in flow structures and energy reduction through compound tsunami mitigation system with embankment and lined piles. Ocean Eng. 164, 722-732, 2018.

Ikezawa, H., Shimozono, T., Sato, S., Depth-integrated non-hydrostatic model for levee overflow, J. JSCE Coastal Eng. (B2) 71 (2), I_7–I_12, 2015 (in Japanese with English abstract).

Fritz, H. M. and Hagar, W. H.: Hydraulics of Embankment Weirs, Journal of Hydraulic Eng., Vol. 124, No. 9, pp.963-971, 1998.

Hayashi, S., Narita, Y., Koshimura, S., Developing tsunami fragility curves from the surveyed data and numerical modeling of 2011 Tohoku Earthquake Tsunami, J. JSCE Coastal Eng. (B2) 69 (2), I_386–I_390, 2013 (in Japanese with English abstract).

Honma, H., Coefficient of flow volume on low overflow weir (I). Proceeding of JSCE, 26(6), pp. 635-645, 1940.

Honma, H., Coefficient of flow volume on low overflow weir (II). Proceeding of JSCE, 26(9), pp. 849-862, 1940.

Kawasaki, K., Ono, T., Piamsa-nga, N., Atsuta, H., Nakatsuji, K. Development of depth-averaged inundation flow model based on CIP method and SMAC method. Proceedings of Hydraulic Engineering, 48, 565-570, 2004 (in Japanese with English abstract).

Nadaoka, K. and Yagi, H. Shallow-water turbulence modeling and horizontal large-eddy computation of river flow. J. Hydraul. Eng. 124 (5), 493–500, 1998.

Ministry of Land, Infrastructure, Transport, and Tourism (MLIT). White paper on land, infrastructure, transport and tourism in Japan, 2011. (URL: https://www.mlit.go.jp/english/white-paper/2011.pdf)

Strusińska-Correia, A. Tsunami mitigation in Japan after the 2011 Tōhoku Tsunami. International journal of disaster risk reduction, 22, 397-411, 2017.

Tanaka, N., Igarashi, Y. Multiple defense for tsunami inundation by two embankment system and prevention of oscillation by trees on embankment, APD-IAHR, Colombo, Sri Lanka, 2016.